

Effects of electron beam generated lattice defects on the periodic lattice distortion structure in 1T-TaS₂ and 1T-TaSe₂ thin layers

Kinyanjui, M. K.; Björkman, T.; Lehnert, T.; Köster, J.; Krasheninnikov, A.; Kaiser, U.;

Originally published:

January 2019

Physical Review B 99(2019), 024101

DOI: <https://doi.org/10.1103/PhysRevB.99.024101>

Perma-Link to Publication Repository of HZDR:

<https://www.hzdr.de/publications/Publ-28802>

Release of the secondary publication
on the basis of the German Copyright Law § 38 Section 4.

Effects of electron beam-generated lattice defects on periodic lattice distortion structure in 1T-TaS₂ and 1T-TaSe₂

M. K. Kinyanjui¹, T. Bjorkman², T. Lehnert¹, J. Koster¹, A. Krasheninnikov^{3,4}, U. Kaiser¹

¹Central Facility of Electron Microscopy, Ulm University, Ulm, Germany

²Department of Natural Sciences, Åbo Akademi, Turku, Finland

³Institute of Ion Beam Physics and Materials Research, Helmholtz-Zentrum Dresden-Rossendorf, Dresden, Germany

⁴Department of Applied Physics, Aalto University, 00076 Aalto, Finland

Abstract

We have investigated the influence of electron beam-generated lattice defects on the structure of the periodic lattice distortion (PLD) which accompanies charge wave modulations in 1T-TaS₂ and 1T-TaSe₂. The Lattice defects were generated through high energy electron beam irradiation in a transmission electron microscope. Using atomic resolved high resolution transmission electron microscopy imaging we directly visualize the structure of the periodic lattice distortion and show the formation of dislocation-like defects as well as the loss of long range order with increased exposure to the electron beam. We also performed density functional calculations in order to understand defect formation in charge density wave modulated 1T-TaSe₂ and 1T-TaS₂ single layers. The formation energy of S and Se point defects is found to be lowest for the S/Se sites in the vicinity of the highly distorted atomic sites and highest at the less distorted atomic site. This points towards a preferential creation of S/Se point defects at the highly distorted atomic sites.

I. Introduction

Charge density waves (CDW) are periodic modulations of charge density which arise due to instabilities in the Fermi surface of low dimensional metals.¹ The CDW state is characterized both by a charge density wave as well as a periodic lattice distortion (PLD) which is the modulation of atomic positions.¹⁻³ The modulation wave vector is given by $\mathbf{q} = 2\mathbf{K}_F$ where \mathbf{K}_F is the Fermi wave vector. A one-dimensional CDW can therefore be described as²

$$\rho(x) = \rho_0 + \rho \cos(qx + \phi(x)) \quad (1)$$

Where $\rho(x)$ is the modulated charge density, ρ_0 is the background charge density, ρ is the CDW amplitude, \mathbf{q} is the wave vector of the CDW, and $\phi(x)$ is the CDW phase. In most cases the CDW distortion is also characterized by metal-to-insulator transitions.¹ Quasi two-dimensional (2D) transition metal dichalcogenides (TMDC) including 1T/2H-TaSe₂, 1T/2H-TaS₂, 2H-NbSe₂ are some of the low dimensional metals that exhibit strong CDW distortions whose transition temperature and commensuration varies mainly with temperature.¹ Experimentally, the CDW can be probed directly using Scanning Tunnelling Microscopy (STM).⁴⁻⁶ On the other hand, diffraction and imaging techniques such as High Resolution and Scanning Transmission electron Microscopy (HR(S)TEM)⁷⁻⁹, electron diffraction¹⁰⁻¹³, neutron and x-ray diffraction¹⁴⁻¹⁶ are only sensitive to the modulation of atomic positions (PLD) that accompanies a CDW distortion.

The CDW condensate has been shown to move in an electric field thus contributing to the transport properties of the CDW material.^{1-3, 17, 18} Theory has predicted that an incommensurate CDW should exhibit frictionless sliding in an electric field,

leading to a Fröhlich type superconductivity.^{2,18} Fröhlich superconductivity is difficult to achieve since the sliding CDW is often pinned by impurities and defects.^{2,17-19} Therefore to understand the transport properties of CDW materials it is also crucial to investigate the interaction of the CDW with crystalline defects and impurities. Interaction of CDW with defects has been investigated indirectly through transport measurements²⁰ and x-ray diffraction²¹⁻²³, as well as directly through real space imaging with STM imaging.²⁴⁻²⁷ In most cases these studies have mainly focused on the effects of impurities introduced through cation doping on the CDW state.²⁸ Little attention has been directed towards the effects of anion point defects. Here we present a study where the in-situ defect generation capabilities of the TEM have been used to create lattice defects and the same time determining the effects of these defects on the CDW state through atomically resolved real space imaging.

The defect creation mechanisms in the TEM arise from the interactions of the sample with the fast electrons. This may include defect creation through electronic excitations (ionization) or by elastic collisions of the fast electrons with the lattice atoms (Knock-on).²⁹⁻³² Other interaction mechanisms include local heating and charging in insulating compounds.²⁹ The ionization damage mechanism is dominant at low electron energies.²⁹ At higher electron energies the generation of vacancies is mostly through the knock-on mechanism.²⁹ It has been shown that at low electron beam energies > 100 kV, the defects caused by electron beam irradiation in transition metal dichalcogenides (TMDCs) include mostly single chalcogen vacancies, divacancies, self-interstitials and extended defects.³⁰ In addition, calculations have also shown that the knock-on threshold for heavier atoms including Ta, Mo and Nb atoms, is at high electron energies in the

order of 500 keV.³⁰ Therefore, the nature of the atoms and the electron beam energy plays a role in determining which atoms are displaced. In the case of 1T-TaS₂/TaSe₂ the large mass difference between the sulfur and tantalum atoms means sulfur and Se atoms are selectively displaced before the Ta atoms.^{30, 31} Regardless of the defect creation mechanism, the created defects can migrate, interact, and condense to form extended defects like dislocations, voids, or defect clusters. Mutka et al showed the capability of electron irradiation on the creation of defects in 1T-TaS₂ using extremely high energy electrons in the order of 2 MeV.³² However, these very high energy electrons knock out both the Ta and S atoms from the lattice leading to rapid amorphisation of the sample. We use a much lower electron voltage of 80 keV which is much lower than the knock-out threshold of the Ta atom.

The TEM based atomically-resolved imaging approach presented in this paper presents several advantages. These include (1) the ability to visualize and analyze the PLD directly through real space mapping of atomic distortions as well as the atomic structure of the underlying lattice.⁷ (2) HRTEM imaging is best suited for imaging CDW properties in free-standing single layers.⁸ (3) TEM experiments can be used for in-situ generation of point defects through controlled use of a specific electron dose, exposure time, and kinetic energy of the electron beam.^{30, 32} (4) The CDW condensate can be considered to be an independent electronic crystal with crystalline-like response to defects or strain/stress through elastic deformation and formation of dislocations, or domain boundaries.^{2,33} Observation of CDW/PLD dislocations has been difficult and has been mainly been achieved through indirect x-ray diffraction methods.²² Recently atomic resolved scanning transmission electron microscopy (STEM) has been used to

successfully image CDW topological defects and phase disorder in charge ordered $\text{Bi}_{0.35}\text{Sr}_{0.18}\text{Ca}_{0.47}\text{MnO}_3$.³⁴ As we show in this paper, real space imaging of the PLD with HRTEM can provide a method to observe these effects as well the elastic response of the CDW to lattice defects arising from electron beam in the TEM.

II. Experimental methods and analysis

A. HRTEM Imaging

In this paper we focused on a few-layers to multi-layer thick 1T-TaS₂ and 1T-TaSe₂ samples obtained through mechanical exfoliation. The choice of this sample thickness was motivated by the fact that single layers of 1T-TaS₂ and 1T-TaSe₂ materials are readily oxidized which leads to the suppression of the CDW.⁸ HRTEM imaging was performed on a FEI Titan 80-300 TEM equipped with an objective lens spherical aberration corrector and operated at 80 kV. During HRTEM imaging a small negative aberration coefficient (Cs) value of -20 μm and small positive focus were used. The cooling experiments were conducted using a Liquid Nitrogen cooled sample holder capable of reaching temperatures of down to ~ 90 K. To investigate the effects of electron-beam generated defects on the CDW/PLD, successive HRTEM images were obtained from the same sample region over time and at a constant electron dose rate in the order of 10^{-6} e⁻/ nm²/s. The exposure time for the acquisition of the HRTEM images was in the order of 1 sec.

B. Visualizing and analyzing the periodic lattice distortion (PLD)

1. Structure of the PLD distorted 1T-TaSe₂/1T-TaS₂

Both bulk 1T-TaS₂ and 1T-TaSe₂ show commensurate CDW/PLD modulation characterized by a $\sqrt{13} a_0 \times \sqrt{13} a_0$ superlattice (a_0 = lattice parameter) at 180 K and

300 K respectively.¹ The atomic structure of the PLD distorted 1T-TaS₂ /1T-TaSe₂ is described in terms of clusters of displaced Ta atoms known as star-of-David clusters.¹⁴ In Fig. 1 the solid lines show individual single star-of-David clusters consisting of 13 Ta atoms. The dotted lines display the $\sqrt{13} a_0 \times \sqrt{13} a_0$ superlattice which connects four star-of-David clusters.

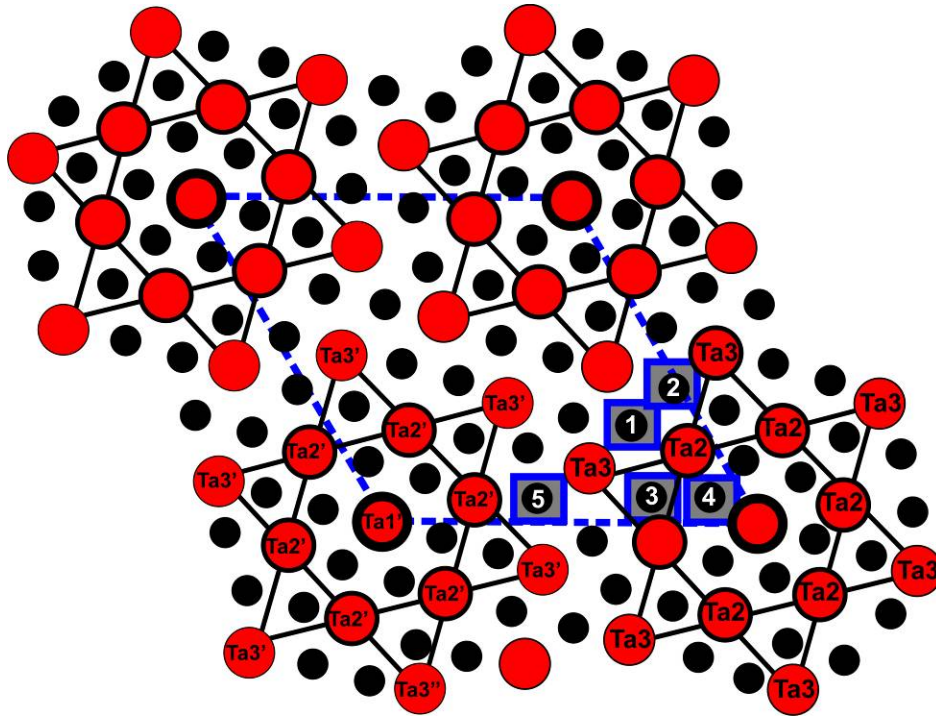


FIG. 1. A schematic showing the atomic structure of the PLD distorted 1T-TaSe₂. The solid lines show single star-of-David cluster consisting of 13 Ta atoms. The dotted line shows the superlattice which connects four star-of-David clusters. Ta atoms are depicted using large open circles While Se atoms are depicted using small solid circles. The inequivalent Ta sites are labeled, Ta1, Ta2, Ta3. The inequivalent Se sites are marked with a square and labeled 1-5 for Se positions Se1-Se5 respectively.

The PLD modulation results in three inequivalent Ta positions labeled as Ta1, Ta2, Ta3. Ta1 is at the center of a 13 Ta atom cluster; there are six Ta2 which are connected to the Ta1 within the same cluster, and the Ta3 which is at the apex of the star-of-David cluster.¹⁴ The maximum Ta displacement is found at position Ta3. The Ta1 atom found at the center of the cluster shows no displacement. The PLD distortion also gives rise to the displacement of Se atoms in a manner similar to Ta atom displacement. This results in five Se inequivalent sites labeled Se1-Se5 in Fig. 1.

2. HRTEM analysis of the periodic lattice distortion

HRTEM imaging and electron diffraction are sensitive to the modulation of atomic positions (PLD) that accompanies a CDW distortion.^{1, 7} In strongly distorted CDW materials, the effects of atomic displacements associated with the PLD state can be therefore be visualized in real space in atomically resolved HRTEM images or in diffraction (Fourier) space. Figure 2(a) displays a HRTEM image from a PLD distorted 1T-TaSe₂ layer. The HRTEM image displays the Ta atomic sublattice characterized by a bright, dark contrast modulation of the Ta atom columns due to the PLD/CDW. The corresponding Fast Fourier Transform (FFT) of the HRTEM image is displayed in Fig. 2(b). The FFT pattern is characterized by a central peak, main reflections from the main 1T-TaSe₂ structure, and superlattice spots due to the PLD modulation. The main reflections (solid circles) and the central spot are (solid circles) surrounded by six superstructure spots (dotted circles). These superstructure reflections, q_1 , q_2 , q_3 surrounding the central spot are shown schematically in Fig. 2(c). These superlattice reflections arise from three charge density waves with wave vectors $q_1, q_2, q_3 = 2\mathbf{K}_F$ where \mathbf{K}_F is the Fermi wave vector and $|\mathbf{q}_{i=1,2,3}| = \sqrt{13} a_0$ where a_0 is the lattice

parameter.¹ The lattice parameters for 1T-TaSe₂ and 1T-TaS₂ are 3.477 Å and 3.346 Å respectively.

By selecting, and masking the satellite spots q_1, q_2, q_3 with a circular Gaussian mask (shown by dotted circles in Fig. 2(c)) followed by inverse FFT, it becomes possible to visualize the PLD as a lattice. Figure 2(d) displays a periodic image showing the positions of the PLD maxima and minima. In the image the bright and dark regions correspond to the maxima and minima of the PLD respectively. The distance between respective PLD maxima/Minima corresponds to $|\mathbf{q}_{i=1,2,3}| = \sqrt{13} a_0$

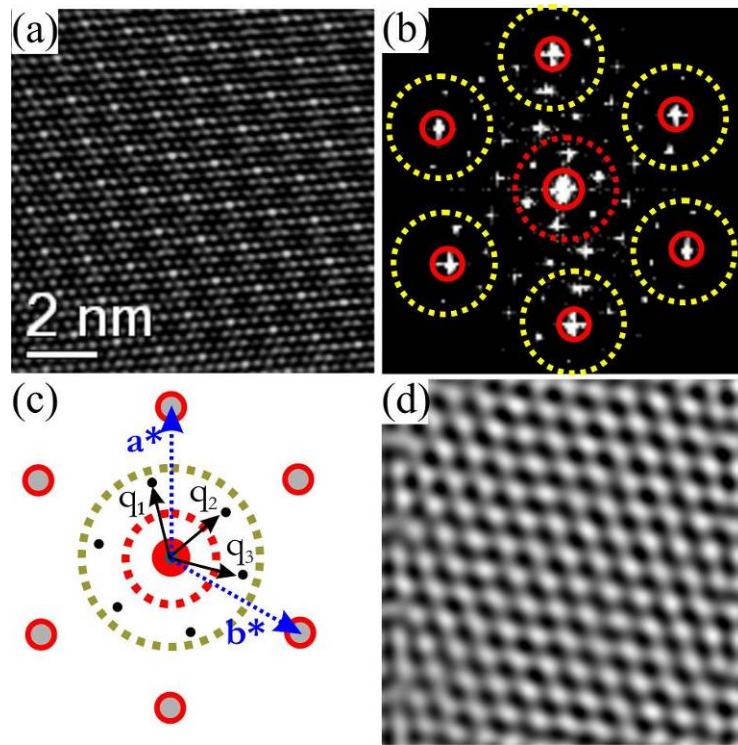


FIG. 2. (a) HRTEM image of 1T-TaSe₂ layer at 300 K. The image is characterized by dark, bright modulation of intensity due to the periodic lattice distortion (b) Fast Fourier Transform (FFT) of the HRTEM image showing the central spot and main reflections from 1T-TaSe₂ structure (solid circles) surrounded by six superlattice spots (dotted circle)

(c) a schematic of the FFT showing the central spot, and the superlattice spots q_1 , q_2 , q_3
(d) PLD lattice obtained after using a circular Gaussian mask to select the superlattice reflections q_1 , q_2 , q_3 followed by inverse FFT.

Theory has shown that a CDW/PLD condensate can be considered to be a deformable electron crystal.^{2,33} This means that the CDW/PLD condensate shows a strain response similar to real crystals. Isolating the PLD lattice from the HRTEM image of PLD distorted 1T-TaSe₂ enables the analysis of the PLD using the powerful Geometrical phase analysis (GPA). GPA methods have been successfully used to analyze strain and deformations at the atomic level in an HRTEM images.^{35, 36} ² Using a mask placed around individual superlattice spots q_i in the FFT pattern of a PLD distorted 1T-TaSe₂, fringe (Amplitude) and phase images from individual superlattice reflections can be calculated.^{35, 36} This is possible since the PLD structure shown in Fig. 2(d) can be considered to be made up of individual lattice fringes due to periodicities q_1 , q_2 , and q_3 . The calculated fringe images therefore show lattice fringes corresponding to the periodicities q_i in the PLD structure. The phase image on the other hand shows the variations in the position of lattice fringes as well as discontinuities in the lattice. In a PLD without any structural changes and defects, the phase of the respective fringes will be constant. Structural changes within the PLD will cause variation in the corresponding periodicities in the fringe image and consequently introducing a phase shift.

Figures 3(a)-(c) display the individual fringes corresponding to periodicities q_1 , q_2 , and q_3 in the PLD while figs. 3(c)- (f) present the respective phase images. These phase and fringe images were obtained from the using the superlattice reflections q_1 , q_2 , q_3 from

the FFT pattern shown in Fig. 2(b). Since the structure of the PLD distorted 1T-TaSe₂ is without any defects, the fringe and phase images from periodicities q_1 , q_2 , and q_3 are constant. The constant intensity in the phase images in Fig. 3(d), (e) and (f) therefore shows that there is no change in the structure of the PLD or discontinuities in the PLD.

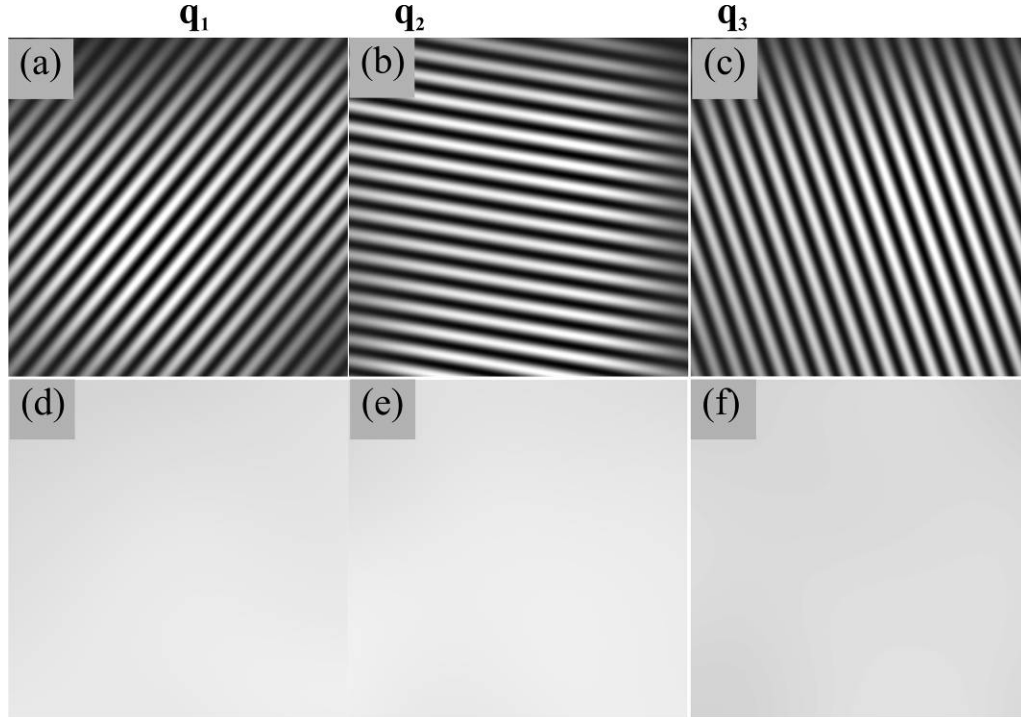


FIG. 3. (a)-(c) Fringes and (d)-(f) phase images associated with the periodicities q_1 , q_2 , and q_3 in the PLD lattice. The constant intensity in the phase image shows that there is no change in the structure of the PLD

C. Density functional calculations

We performed density functional theory (DFT) calculations in order to determine the formation energy of single S and Se point defects in CCDW/PLD distorted 1T-TaS₂ and 1T-TaSe₂ respectively. The formation energies were then calculated for different S

and Se positions in PLD modulated 1T-TaS₂ and 1T-TaSe₂. These positions are indicated as squares in Fig. 1. DFT calculations were performed with the projector augmented wave (PAW) method³⁷ using the Vienna ab initio simulation package (VASP)³⁸ employing the VASP 2012 PAW sets.^{38,39} A plane wave basis cutoff of 400 eV was used and results were unchanged to within the 0.1 eV upon decreasing this to 300 eV. Defect formation energies of the CDW phase were calculated in 5x5 supercells with 975 and 675 atoms in the pristine cell, for the T and H phases, respectively, using only the Γ -point for sampling the Brillouin zone. The atomic positions were relaxed until the maximal residual force was smaller than 5 meV/Å. The formation energies were calculated with respect to the Se chemical potential of the Se dimer. All energies compared were calculated in the same supercells, to minimize errors.

II. Results and Discussion

A. Effects of electron irradiation on the periodic lattice distortion

1. Disorder in the PLD

To investigate the effects of electron beam irradiation on the PLD successive HRTEM images were obtained from the same sample region in 1T-TaSe₂ and 1T-TaS₂ samples. The electron dose was kept constant and only the exposure time was varied. Figure 4(a) displays a HRTEM image from a few layers of 1T-TaS₂ obtained at 300 K. The corresponding FFT pattern is displayed in Fig. 4(b). The FFT image displays the main reflections from 1T-TaS₂ structure as well as the super-lattice spots arising from the nearly commensurate CDW (NCCDW) modulation characteristic of 1T-TaS₂ at 300 K. Figure 4(c) displays the same sample region after a few seconds of exposure to the

electron beam. The corresponding FFT image after beams exposure is displayed in Fig. 4(d).

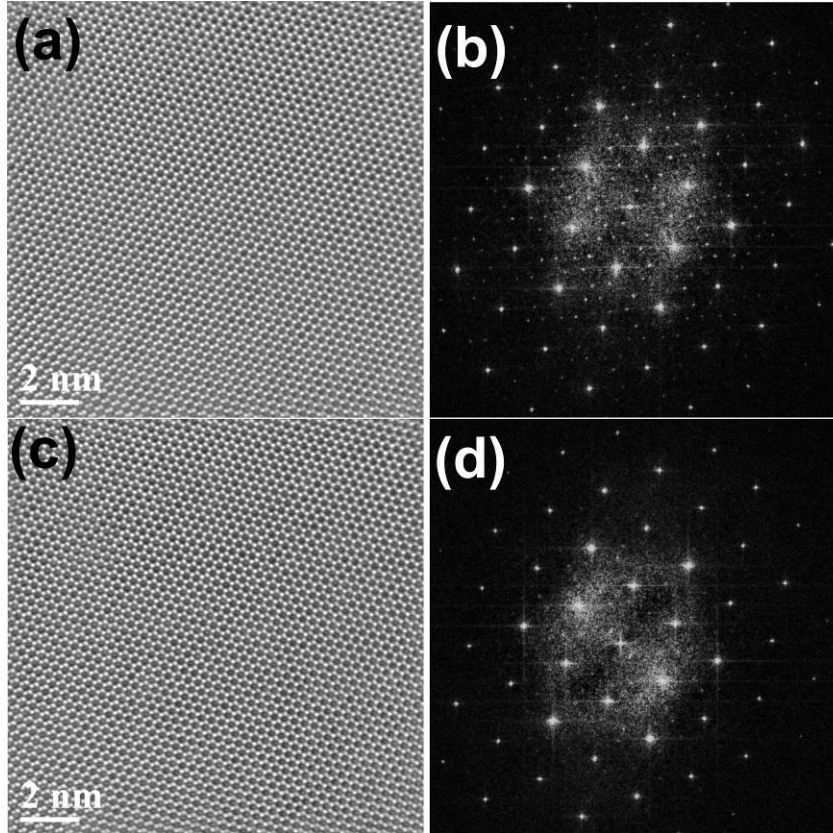


FIG. 4. (a) HRTEM image from a few layers of 1T-TaS₂ obtained at 300 K (b) FFT image showing the main reflections and the superlattice reflections from the nearly commensurate CDW (NCCDW) modulation (c) after a few seconds exposure to the electron beam. (d) FFT after exposure to the beam. The superlattice spots from NCCDW have largely disappeared but the spots from the main structure are still visible.

In the FFT obtained after exposure to the electron beam, we observe that the superlattice reflections from the NCCDW have become more diffuse but the main reflections from the 1T-TaS₂ structure are largely unchanged. At the same the HRTEM images in Fig. 4(a)

and (c) show that the main structure is still intact. Similarly, we explored the evolution of CDW structure in commensurately CDW distorted 1T-TaSe₂ with exposure to the electron beam.

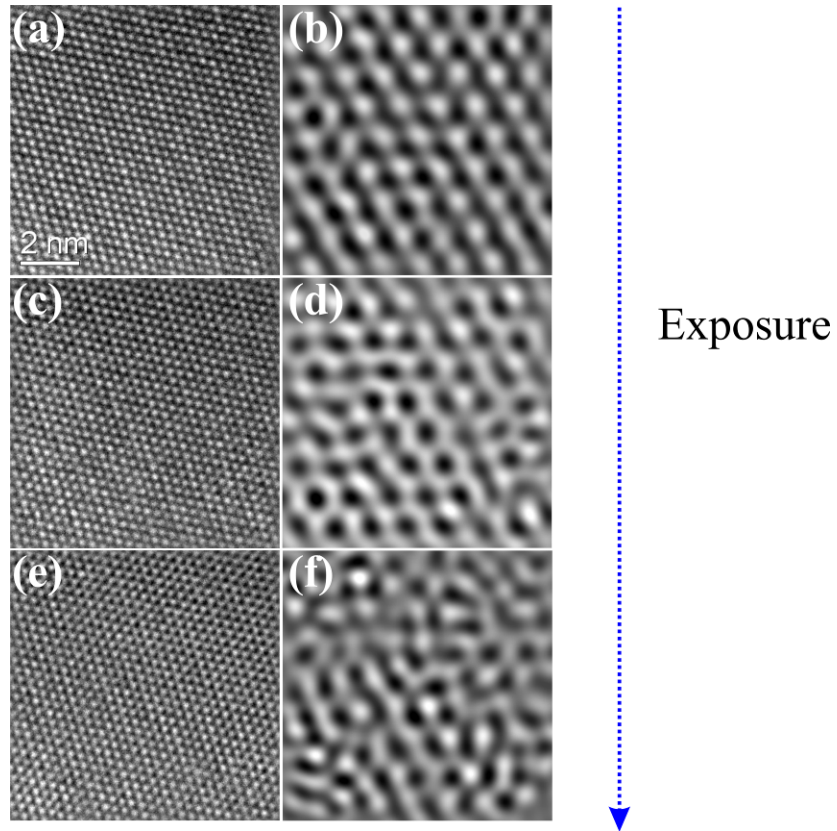


FIG. 5. (a), (c), (e) Successive HRTEM images obtained at 300 K from a 1T-TaSe₂ layer over time at a constant electron dose. The PLDs in (b), (d), (f) correspond to the HRTEM images in (a), (c), and (e) respectively.

Figures 5(a), (c), (e) show successive HRTEM images from the 1T-TaSe₂ sample obtained at 300 K. Similar to the 1T-TaS₂ layers, the HRTEM images from the 1T-TaSe₂ layers were also obtained at a constant electron dose over time and from the same sample

region. By using the method to visualize the PLD from the HRTEM images elucidated in the previous section, respective PLD were also obtained after every exposure. The PLDs shown in Figs. 5(b), (d), (f) which correspond to the HRTEM images in figs. 5(a), (c), and (e) respectively. It can be clearly seen that with increased beam exposure the respective PLD structure shows increasing disorder. On the other hand, the respective Ta sublattices shown in the HRTEM images do not show any changes. A radial distribution function (RDF), $g(r)$, can be used to demonstrate the evolution of the PLD lattice disorder with increased exposure to the electron beam. The RDF shows the periodicities in the PLD lattice in terms of distance to the nearest and next-nearest PLD maxima.

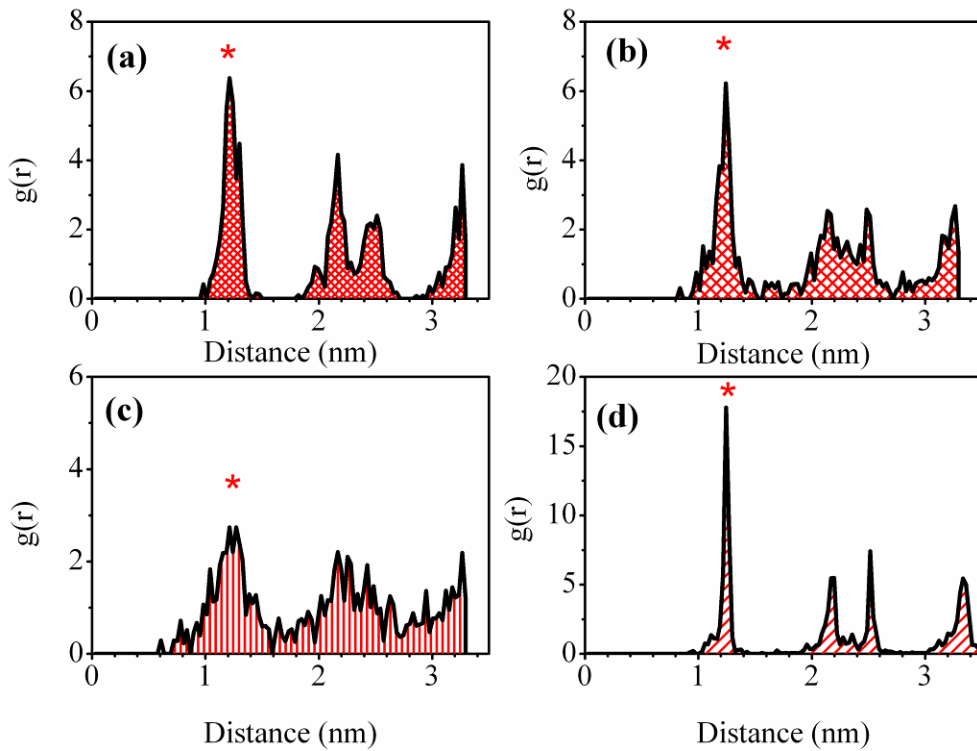


FIG. 6 (a)-(c) Radial distribution functions (RDF), $g(r)$, showing the distances between the nearest and next-nearest maxima in the PLD lattices shown in Figs. 5(b), (c) and (f)

respectively. (d) RDF of PLD for a simulated HRTEM image of 1T-TaSe₂ without any irradiation damage

A RDF from a simulated CCDW distorted 1T-TaSe₂ without any irradiation damage is shown in Fig 6(d) for comparison. The peaks marked with an asterisk show the main periodicity corresponding to the distance between neighbouring PLD maxima which is also equal to the modulation wave vector $|q_{i=1,2,3}| = \sqrt{13} a_0$. With increasing exposure to the electron, the RDF is then characterized by broadening peaks at large periodicities. The broadening of the peaks shows a loss of long range order in the structure of PLD with the increased exposure time to the electron beam.

2. Defects within the PLD

Using the procedure introduced in previous section, we also calculated fringe and phase images from respective superlattice spots to monitor the evolution of PLD structure with increased exposure to the electron beam. Figures 7(a)-(c) display fringe images showing the periodicities q_1 , q_2 , and q_3 present in the PLD structures shown in Fig. 5(b), (d), and (f). In particular the fringe images show the changes in individual periodicities q_1 , q_2 , and q_3 with increased exposure of the PLD structure to the electron beam. We observe two effects of increasing beam exposure to the lattice fringes (1) The fringes become more bended (2) appearance of dislocation-like defects. In Fig. 7 the dislocation-like defects in respective fringes are marked with dotted circles. The dashed square shows regions with bended fringes. The calculated phase image shows the structure in the vicinity of the dislocation-like defects in the PLD. This is displayed in figs. 8(a) and (b) where the PLD dislocation and its phase image are displayed respectively.

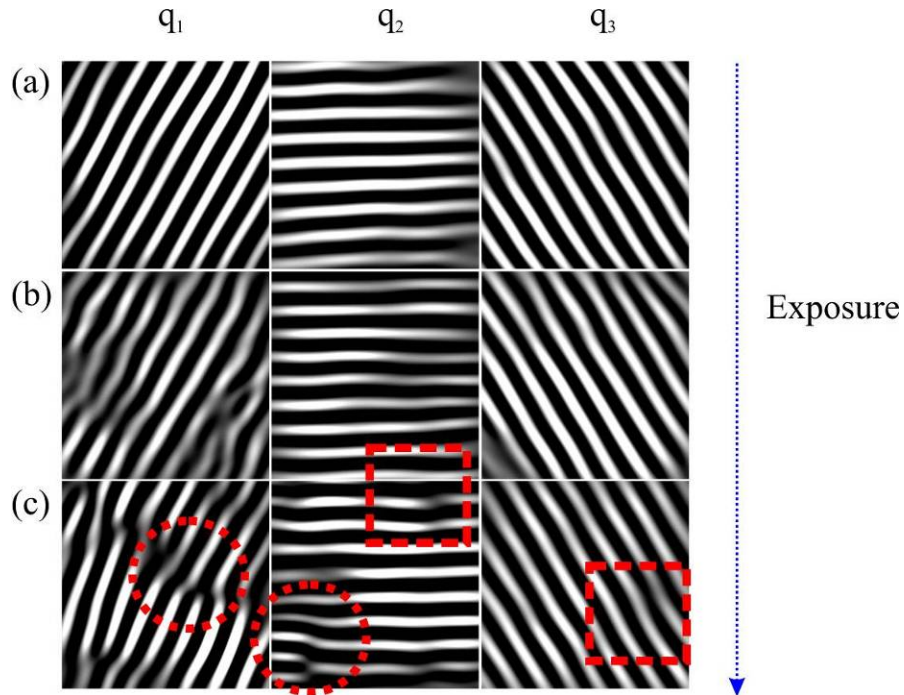


FIG. 7. (a)-(c) Fringe corresponding to periodicities q_1 , q_2 , q_3 in the PLD structure shown in Figs. 5 (b)-(g) respectively. The fringes show changes associated with increased exposure to the electron beam. The defects within the PLD in form of dislocations are marked with dotted circles. The dashed square shows regions with bended fringes

The grey scale in the phase image varies from dark to bright which represents a change of 2π in the phase at the dislocation. The PLD is therefore significantly distorted in the vicinity of the dislocation-like defect. This distortion leads to the displacement in the position of the lattice fringes in the PLD. We have observed two main electron beam induced effects on the PLD. These include formation of dislocation-like topological defects in the PLD structure and increased disorder. It is important to note that dislocation-type defects shown in Figs. 7 and 8 and the disorder shown in Fig. 6 are a characteristic of the PLD and not the underlying atomic lattice.

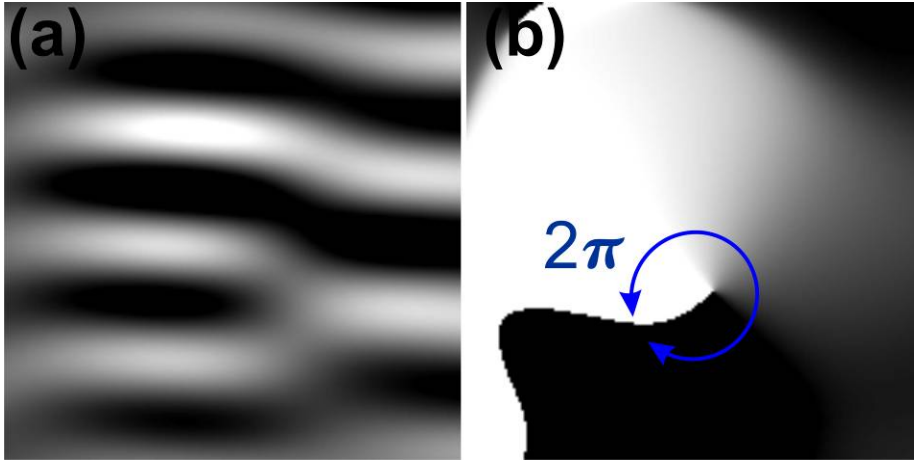


FIG. 8. (a) A fringe image obtained from superlattice reflections q_2 showing a dislocation in the PLD structure in greater details (b) a phase image showing the variations in the position of lattice fringes in the PLD at the vicinity of the dislocation. The grey scale in the phase image varies $0-2\pi$.

The observed dislocations in the PLD structure and the disorder are due to the interaction of the CDW with the lattice defects generated in CDW modulated 1T-TaSe₂ structure by the electron beam. The interaction of the CDW with lattice defects has been explained in terms of the interaction between the CDW and Friedel oscillations associated with the defects.^{21, 32, 40-45} In metals, point defects cause a local Fermi surface instability which results in damped oscillations of the charge density around the defect.⁴⁰ The local Friedel oscillations has a period $\sim 2K_F$ where K_F is the Fermi wave vector.^{21, 43} In metallic and CDW distorted dichalcogenides, the point defects and impurities also result in local Friedel oscillations which also have the same period as the CDW distortion.⁴⁶ The interference of the CDW and the Friedel oscillations leads to the phase of the CDW being pinned locally at the defect. In this present case, the irradiation with electron beam

creates point defects (single Se/S vacancies) that pin the phase of the CDW locally. The pinning induces strain in the CDW lattice since the CDW reacts elastically by deforming around the defect. With increase in the concentration of defects, elastic deformation is not longer enough to overcome the pinning energy and this leads to the formation of CDW topological defects such as dislocations.⁴⁴⁻⁴⁷ The number of these CDW defects will increase rapidly with increasing concentration of irradiation defects. With increasing number of defects CDW breaks into domains thus losing its long range order.⁴⁷

B. Defect formation in PLD distorted 1T-TaS₂ and 1T-TaSe₂ single layers

The process of electron beam initiated defect formation in most TMDCs has been shown to proceed through creation of single chalcogen vacancies and divacancies.^{30-32, 48-52} As the density of these single vacancies increases, defect clustering as well as the formation of extended line defects is then observed. We calculated the formation energies of S and Se single vacancies in PLD distorted 1T-TaSe₂ and 1T-TaS₂ monolayers. The formation energies were calculated for different S and Se positions in CDW/PLD modulated 1T-TaS₂ and 1T-TaSe₂ single layers. These S/Se positions are labeled as Se1, Se2, Se3, Se4, Se5 and are indicated as squares in Fig. 1. The positions of the respective single Se vacancies with respect to the distorted structure and PLD are shown in Fig. 9 for a single layer CCDW distorted 1T-TaSe₂. In Fig. 9(a) we display a calculated HRTEM image for CCDW distorted 1T-TaSe₂ single layers without any defects. The $\sqrt{13} a_0 \times \sqrt{13} a_0$ superlattice due to the PLD modulation is indicated by the dotted parallelogram. A star-of-David cluster consisting of 13 Ta atoms (large solid spheres) and Se atoms (small solid spheres) is also shown.

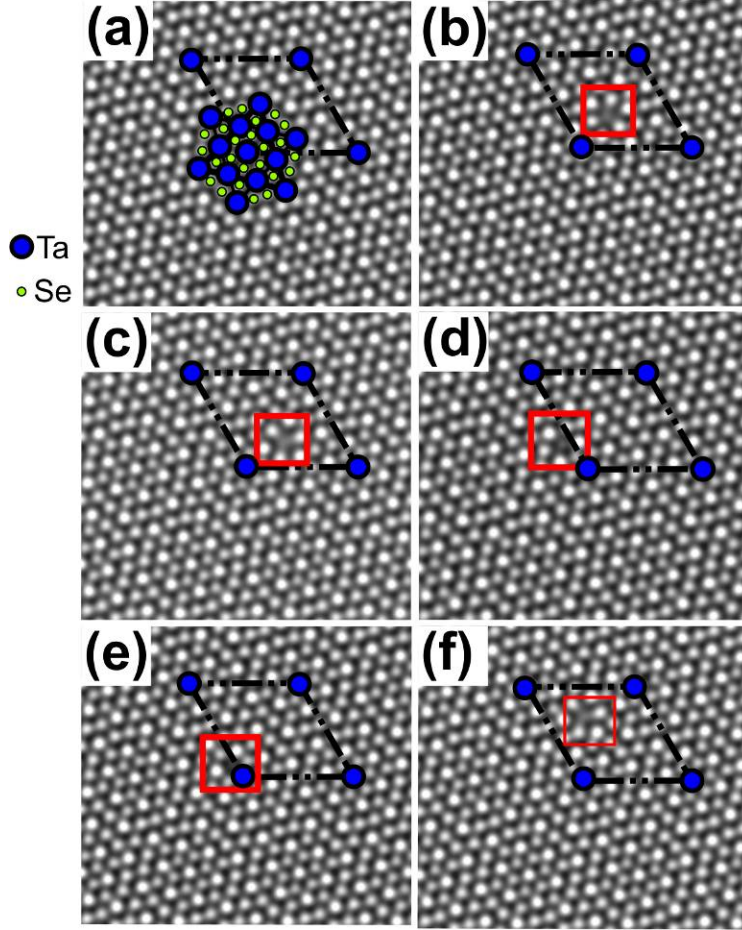


FIG. 9 Calculated HRTEM image from a PLD distorted 1T-TaSe₂ single layer. The $\sqrt{13}a_0 \times \sqrt{13}a_0$ superlattice due to the CDW/PLD is shown by the dotted parallelogram. The star-of-David cluster consisting of 13 Ta atoms (large solid spheres) is also indicated (b)-(f) Single Se vacancies at the Se atom positions 1-5 respectively.

In Figs. 9(b)-(f) we show calculated HRTEM images for a CCDW distorted 1T-TaSe₂ single layer with single Se vacancies at Se positions Se1, Se2, Se3, Se4 and Se5 respectively. The positions of Se single vacancies in the HRTEM images are marked with squares. The corresponding formation energies of single S and Se vacancies at various inequivalent positions indicated in Fig 9 are shown in Table 1.

Se atom position	TaSe ₂ , energy (eV)	TaS ₂ , energy (eV)
1	1.8	2.3
2	1.9	2.4
3	3.1	3.1
4	2.8	3.0
5	1.5	2.2

Table 1: Formation energies of single S and Se vacancies for different Se and S sites in a PLD distorted 1T-TaSe₂ and 1T-TaS₂ lattice

As can be deduced from the table 1, atomic positions Se1, Se2, Se5 have lower vacancy formation energy than positions Se3, Se4. As can be observed in Figs. 9 positions Se1, Se2, Se5 are at/near the maxima of the PLD and while positions Se3, Se4 are at/near the minima of the PLD. This is also the case with PLD distorted 1T-TaS₂ structure. This can be explained by the fact that the Ta and Se/S atoms at the PLD maxima have undergone the most distortion from their equilibrium positions with respect to the undistorted structure.²⁰ In PLD distorted 1T-TaS₂ and 1T-TaSe₂ structures the atoms that have undergone most displacement are near the vicinity of the Ta3 at the apex of the star-of-David cluster. It is therefore energetically more favorable to create defects at these highly distorted sites. Therefore, the formation energy of S and Se single vacancies is much lower at these highly distorted sites. On the other hand, atoms at the vicinity of the PLD minima have undergone the least displacement. This corresponds to the atoms in the

vicinity of Ta1 center of a star-of-David cluster. Consequently, the formation energy of S and Se single vacancies is much higher at these less distorted S and Se sites.

III. Conclusion

We have investigated the influence of electron beam-generated lattice defects on the structure of the periodic lattice distortion (PLD) which accompanies charge wave modulations in 1T-TaS₂ and 1T-TaSe₂. We have exploited the in-situ defect generation capabilities of the electron beam in a transmission electron microscope to create point defects and the same time determining the effects of these defects on the structure of the PLD in CDW modulated 1T-TaS₂ and 1T-TaSe₂. This is possible because electron diffraction and atomically resolved imaging (HRTEM) capabilities of the TEM can probe the structure of the periodic lattice distortion (PLD) which is a modulation of the atomic position that accompany the CDW. We observe the formation of dislocation-like topological defects in the PLD structure as well as the loss of CDW long range order with increased exposure to the electron beam. In addition, we use density functional calculations to understand defect formation in PLD distorted 1T-TaS₂ and 1T-TaSe₂ monolayers. The formation energy of sulfur (S) and selenium (Se) point defects is found to be lowest for the S/Se sites in the vicinity of the highly distorted atomic sites and highest at the less distorted atomic site. This points towards preferential creation of S/Se point defects at the highly distorted atomic sites in CDW modulated 1T-TaS₂ and 1T-TaSe₂.

Acknowledgements.

We wish to thank O. Lehtinen for fruitful discussions and valuable suggestions. The authors acknowledge funding from the German Research Foundation (DFG) and the

Ministry of Science, Research and the Arts (MWK) of the federal state Baden-Württemberg, Germany in the frame of the SALVE (Sub-Angstroem Low-Voltage) project.

References

- ¹J. Wilson, F. D. Salvo, and S. Mahajan, *Adv. Phys.* 24, 117 (1975).
- ²P. Monceau, *Adv. Phys.* 61, 325 (2012).
- ³R. H. Friend, and D. Jerome, *J. Phys. C: Solid State Phys.* 12, 1441(1979)
- ⁴H. Dai, and C. Lieber, *Annu. Rev. Phys. Chem.* 44, 237 (1993)
- ⁵B. Giambattista, C. G. Slough, W. W. McNairy and R. V. Coleman, *Phys. Rev. B* 41, 10082 (1990).
- ⁶A. Manivannan, L.A. Nagahara, M. Tsukada, K. Hashimoto, A. Fujishima, H. Berger, and F. Levy, *Surf. Sci.* 274, L554 (1992)
- ⁷T. Ishiguro, and H. Sato, *Phys. Rev. B* 52, 759 (1995).
- ⁸A. W. Tsen, R. Hovden, D. Wang, Y. D. Kim, J. Okamoto, K. A. Spoth, Y. Liu, W. Lu, Y. Sun, J. C. Hone, L. F. Kourkoutis, P. Kim, and A. N. Pasupathy, *Proc. Nat. Acad. Sci. U.S.A.* 112, 15054 (2015).
- ⁹D. Sakabe, Z. Liu, K. Suenaga, K. Nakatasugawa, and S. Tanda, *NPJ. Quantum Mater.* 2, 22(2017)
- ¹⁰J. van Landuyt, G. van Tendeloo, and S. Amelinckx, *Phys. Status Solidi A* 26, 197 (1974)
- ¹¹R. L. Whithers and J. W. Steeds, *J. Phys. C* 20, 4019 (1987).
- ¹²K. K. Fung, J. W. Steeds, and J. A. Eades, *Physics B* 99, 47 (1980).
- ¹³C. B. Scruby, P. M. Williams, and G. S. Parry, *Philos. Mag.* 31, 255 (1975).

- ¹⁴ R. Brouwer, and F. Jellinek, *Physica (Amsterdam)* 99B, 51 (1980).
- ¹⁵ A. Spijkerman, J. L. de Boer, A. Meetsma, G. A. Wieggers, and S. van Smaalen, *Phys. Rev. B* 56, 13757 (1997).
- ¹⁶ D. E. Moncton, J. D. Axe, and F. J. DiSalvo, *Phys. Rev. Lett.* 34, 734 (1975).
- ¹⁷ G. Gruner, *Rev. Mod. Phys.* 60, 1129 (1988)
- ¹⁸ H. Frohlich, *Proc. R. Soc. A* 223, 296 (1954)
- ¹⁹ H. Fukuyama, and P. A. Lee, *Phys. Rev. B* 17, 535 (1978).
- ²⁰ J. McCarten, D. A. DiCarlo, M. P. Maher, T. L. Adelman, and R. E. Thorne, *Phys. Rev. B* 46, 4456 (1992).
- ²¹ S. Rouzière, S. Ravy, J.-P. Pouget, and S. Brazovskii, *Phys. Rev. B* 62, R16231 (2000).
- ²² D. Le Bolloc'h, V.L.R. Jacques, N. Kirova, J. Dumas, S. Ravy, J. Marcus, and F. Livet, *Phys. Rev. Lett.* 100, 096403 (2008).
- ²³ E. Pinsolle, N. Kirova, V. L. R. Jacques, A. A. Sinchenko, and D. Le Bolloc'h, *Phys. Rev. Lett.* 109, 256402 (2012).
- ²⁴ S. Brazovskii, C. Brun, Z.-Z. Wang, and P. Monceau, *Phys. Rev. Lett.* 108, 096801 (2012).
- ²⁵ C. J. Arguello, S. P. Chockalingam, E. P. Rosenthal, L. Zhao, C. Gutiérrez, J. H. Kang, W. C. Chung, R. M. Fernandes, S. Jia, A. J. Millis, R. J. Cava, and A. N. Pasupathy, *Phys. Rev. B* 89, 235115 (2014).
- ²⁶ M. Novello, B. Hildebrand, A. Scarfato, C. Didiot, G. Monney, A. Ubaldini, H. Berger, D. R. Bowler, P. Aebi, and C. Renner, *Phys. Rev. B* 92, 081101(R) (2015).
- ²⁷ J. Okamoto, C. J. Arguello, E. P. Rosenthal, A. N. Pasupathy, and A. J. Millis *Phys. Rev. Lett.* 114 026802 (2015)

- ²⁸ F. J. DiSalvo, J. A. Wilson, B. G. Bagley, and J. V. Waszczak, *Phys. Rev. B* 12, 2220 (1975).
- ²⁹ R. F. Egerton, P. Li, M. Malac, *Micron* 35 399(2004)
- ³⁰ H.-P. Komsa, J. Kotakoski, S. Kurasch, O. Lehtinen, U. Kaiser, and A. V. Krasheninnikov, *Phys. Rev. Lett.* 109, 035503 (2012).
- ³¹ Y.Y. Loginov, P.D. Brown, N. Thompson and K. Durose, *Journal of Crystal Growth* 117 682 (1992)
- ³² H. Mutka, *Phase Transitions* 11, 221 (1988); H. Mutka and P. Molinié, *J. Phys. C* 15, 6305 (1982); H. Mutka, N. Housseau, L. Zuppiroli, and J. Pelissier, *Philos. Mag. B* 45, 361 (1982)
- ³³ D. Feinberg and J. Friedel, *J. Phys. (France)* 49, 485 (1988).
- ³⁴ B. H. Savitzky, I. El Baggari, A. S. Admasu, J. Kim, S.-W. Cheong, R. Hovden, L. F. Kourkoutis, *Nat. Comm.* 8, 1883(2017)
- ³⁵ M. J. Hÿtch, E. Snoeck, and R. Kilaas, *Ultramicroscopy* 74, 131 (1998)
- ³⁶ A.K. Gutakovskii, A.L. Chuvilin, and S. A. Song, *Bull. Russ. Acad. Sci. Phys.* 71, 1426 (2007).
- ³⁷ P. E. Blöchl, *Phys. Rev B* 50, 17953 (1994)
- ³⁸ G. Kresse and J. Furthmüller, *Comput. Mater. Sci.* 6, 15 (1996)
- ³⁹ G. Kresse and D. Joubert, *Phys. Rev. B* 59, 1758 (1999)
- ⁴⁰ J. Friedel, *Phil. Mag.* 43, 153(1952)
- ⁴¹ I. Tüttó and A. Zawadowski, *Phys. Rev. B* 32, 2449 (1985).
- ⁴² J. R. Tucker, *Phys. Rev. B* 40, 5447 (1989).
- ⁴³ J. P. Pouget, *C. R. Physique* 17, 332(2016)
- ⁴⁴ L. Zuppiroli, H Mutka, S. Bouffard, *Mol. Cryst. Liq, Cryst.* 85, 1 (1982)
- ⁴⁵ G. Salvetti, C. Roucau, R. Ayroles, H. Mutka, and P. Molinie, *J. Phys. Lett. (Paris)* 46, L507(1985)

- ⁴⁶ H. Mutka, N. Housseau, J. Pelesier, R. Ayroles, and C. Rancau, *Solid State Commun.* 50, 161(1984)
- ⁴⁷ H. Dai, H. Chen, and C. M. Lieber, *Phys. Rev. Lett.* 66, 3183(1991)
- ⁴⁸ H.-P. Komsa, S. Kurasch, O. Lehtinen, U. Kaiser, and A. V. Krasheninnikov, *Phys. Rev. B* 88, 035301 (2013).
- ⁴⁹ H.-P. Komsa, and A. V. Krasheninnikov, *Advanced Electronic Materials* 3, 1600468. (2017)
- ⁵¹ S. S. Wang, G. D. Lee, S. Lee, E. Yoon, and J. H. Warner, *ACS Nano* 10, 5419 (2016).
- ⁵² W. Zhou, X. Zou, S. Najmaei, Z. Liu, Y. Shi, J. Kong, J. Lou, P. M. Ajayan, B. I. Yakobson, and J.-C. Idrobo, *Nano Lett.* 13, 2615 (2013).
- ⁵³ X. Zhao, J. Kotakoski, J. C. Meyer, E. Sutter, P. Sutter, A. V. Krasheninnikov, U. Kaiser, W. Zhou, *MRS Bulletin* 42, 667(2017)